RESEARCH ARTICLE | APRIL 07 2022

$Ti_3C_2T_x$ MXene/Ge 2D/3D van der Waals heterostructures as highly efficient and fast response near-infrared photodetectors

Special Collection: Photodetectors Based on Van der Waals Heterostructures and Hybrid 2D Materials

Chao Xie ; Yi Wang; Siliang Wang ; Wenhua Yang ; Wei Zeng ; Zhixiang Huang; Feng Yan

Appl. Phys. Lett. 120, 141103 (2022)
https://doi.org/10.1063/5.0085690

Applied Physics Letters ARTICLE scitation.org/journal/apl

$Ti_3C_2T_x$ MXene/Ge 2D/3D van der Waals heterostructures as highly efficient and fast response near-infrared photodetectors

Cite as: Appl. Phys. Lett. **120**, 141103 (2022); doi: 10.1063/5.0085690
Submitted: 18 January 2022 · Accepted: 31 March 2022 ·
Published Online: 7 April 2022

Chao Xie,[1,a] Yi Wang,[1] Siliang Wang,[1,a] Wenhua Yang,[1] Wei Zeng,[1] Zhixiang Huang,[1] and Feng Yan[2,a]

AFFILIATIONS

[1]Information Materials and Intelligent Sensing Laboratory of Anhui Province, Industry-Education-Research Institute of Advanced Materials and Technology for Integrated Circuits, School of Electronics and Information Engineering, Anhui University, Hefei, Anhui 230601, People's Republic of China

[2]Department of Applied Physics, Research Institute of Intelligent Wearable Systems, The Hong Kong Polytechnic University, Hong Kong, People's Republic of China

Note: This paper is part of the APL Special Collection on Photodetectors Based on Van der Waals Heterostructures and Hybrid 2D Materials.

[a]**Authors to whom correspondence should be addressed:** chaoxie@ahu.edu.cn; sliang_wang@163.com; and apafyan@polyu.edu.hk

ABSTRACT

Cost-effective and highly efficient near-infrared photodetectors are urgently demanded in many electronic and optoelectronic products for applications in both military and civil areas. Herein, by using a simple solution-based drop-casting technique, we fabricate a $Ti_3C_2T_x$ MXene/Ge two-dimensional/three-dimensional van der Waals heterostructure, which can function well as a highly efficient near-infrared photodetector. When shined by 1550 nm light illumination, the heterostructure exhibits an apparent photovoltaic effect and can, thus, work as a self-driven near-infrared photodetector. A representative photodetector achieves a photocurrent responsivity of ~314.3 mA W^{-1} at zero bias voltage, which can be improved to as high as ~642.6 mA W^{-1} by applying a small reverse bias voltage of −1 V. In addition, other critical performance parameters such as current on/off ratio, specific detectivity, and response speed are estimated to be ~430, ~2.01×10^{11} Jones, and 17.6/13.6 μs, respectively. The excellent device performance is comparable to that of many previously reported two-dimensional material/Ge heterostructure-based near-infrared photodetectors, which cannot be constructed using facile solution-based processes. This work provides a facile avenue for developing high-performance and low-cost near-infrared photodetectors, which will find important applications in future optoelectronic systems.

Near-infrared (NIR) photodetectors are important components of a large number of electronic and optoelectronic products, including NIR optical communication system, night vision reviewer, laser range-finder, remote sensing imaging system, infrared digital camera, and so on.[1–3] Due to the extensive applications of these products in many military and civil fields, developing high-performance and low-cost NIR photodetectors has long garnered special research interest worldwide.[4,5] Nowadays, commercially available NIR photodetectors composed primarily of traditional inorganic semiconductors inevitably suffer from a lot of dilemmas, although relatively good NIR photodetection performance has already been attained with these devices.[6] The dilemmas usually include complex device geometries, strictly required epitaxial conditions for the growth of photoactive materials, complicated multistep manufacturing processes, and high-cost and high-vacuum apparatuses, which render commercial NIR photodetectors uneconomical and also greatly restrict their wide usage and further development. As an alternative, hybrid van der Waals heterostructures made of two-dimensional (2D) layered material/three-dimensional (3D) semiconductor with a narrow bandgap can provide a facile platform for constructing NIR photodetectors with simplified device geometries and easy manufacturing procedures.[7–9] Such hybrid heterostructures normally hold following advantages: (a) improved light absorption efficiency and widened photo absorption spectral region. (b) Efficient separation and transportation of photoinduced charge

carriers with the help of a built-in electric field. (c) Exotic characteristics brought by the synergistic effect of different material components. By using Ge as the underlying 3D semiconductor, NIR photodetectors based on graphene/Ge and 2D transition metal dichalcogenide (TMD)/Ge hybrid van der Waals heterostructures with respectable NIR photoresponse performance (e.g., photocurrent responsivity: 51.8–750 mA W^{-1}) have recently been explored.[10–15] Nevertheless, these devices cannot be prepared using facile solution-based processes, which, to some extent, limits applications with low-cost and multifunctional purposes.

In recent years, MXenes, as a relatively new group of 2D layered materials, have attracted increasingly more research enthusiasm.[16] This class of materials refers to 2D transition metal carbides, carbonitrides, and nitrides and shared general formula $M_{n+1}X_nT_x$ (n = 1, 2, or 3), where M, X, and T_x represent an early transition metal (Ti, Mo, Ta, Cr, etc.), carbon and/or nitrogen, and surface functional groups (−O, −OH, −F, −Cl, etc.), respectively.[17] MXenes are generally obtained through selectively etching away the A atoms from the ternary and layered MAX phases in which A denotes group IIIA or IVA element (Ga, Al, Si, etc.). Due to their distinctive physical, chemical, and mechanical characteristics that can be regulated by different transition metals and surface terminations, these materials have found important applications in many energy and electronic devices such as capacitors,[18] ion batteries,[19] field-effect transistors,[20] transparent conductors,[21] actuators,[22] and so on. Recently, MXenes have also been explored in photosensitive devices, serving as photoabsorbers, transparent electrodes, Schottky contacts, and plasmonic materials, for their appealing electrical and optical properties, including high transparency, saturable absorption, and high electrical conductivity.[23–30] For example, Zhang *et al.* reported on the fabrication of a $Ti_3C_2T_x$ MXene/Si vertical van der Waals heterostructure, which can serve as a self-driven photodetector with a photocurrent responsivity of ∼26.95 mA W^{-1} and response speed of 0.84/1.67 ms.[31] Afterward, by introducing an interfacial SiO_x passivation layer and controlling the MXene thickness, a photodetector based on Ti_3C_2 MXene/Si hybrid heterostructure with improved photocurrent responsivity up to ∼402 mA W^{-1} and peak external quantum efficiency of 60.3% at zero bias has been attained.[32] Very recently, Song and colleagues proposed a $Ti_3C_2T_x$ MXene/GaN van der Waals heterostructure-based ultraviolet photodiode, which can work in a self-driven mode with a large responsivity of ∼284 mA W^{-1}, a high specific detectivity over 10^{13} Jones, and a fast response speed of 7.55 μs/1.67 ms.[33] By using patterned $Ti_3C_2T_x$ MXene films as the transparent electrodes, Luo and coworkers constructed a MXene-GaN-MXene MSM photodetector. Compared with traditional Cr/Au-GaN-Cr/Au MSM photodetectors, the use of MXene electrodes greatly reduced the dark current by three orders of magnitude and, therefore, significantly improved specific detectivity.[34]

Being inspired by the above studies, we herein present a NIR photodetector composed geometrically of a $Ti_3C_2T_x$ MXene/Ge 2D/3D van der Waals heterostructure, which is prepared by a facile solution-based drop-casting method. The as-fabricated heterostructure is able to function as a self-driven photodetector, thanks to the apparent photovoltaic behavior under 1550 nm NIR light illumination. At zero bias, the device reaches a respectable photocurrent responsivity of ∼314.3 mA W^{-1}, and the value can be enhanced to as high as ∼648.6 mA W^{-1} at a small reverse working bias of −1 V. In addition, the NIR photodetector also shows a high current on/off ratio of ∼430, a decent specific detectivity of $\sim 2.01 \times 10^{11}$ Jones, and a fast response speed of 17.6/13.6 μs. The simple device geometry, facile solution-based processability, and distinctive device performance render the present van der Waals heterostructure extremely promising for cost-effective and highly efficient NIR photodetection.

The $Ti_3C_2T_x$ MXene was synthesized by etching Al from Ti_3AlC_2 powders via a minimally intensive layer delamination (MILD) etching method employing LiF/HCl mixed solution as etchant, as described in a previous work.[35] First, the etchant was obtained by adding 0.5 g of LiF to 10 ml of 9 M HCl and kept under continuous stirring until complete dissolution. Then, 0.5 g of Ti_3AlC_2 was steadily added to the above solution, which was kept under magnetic stirring at 40 °C for 24 h to allow complete reaction. Afterward, the obtained mixture was washed with de-ionized (DI) water via centrifugation at 3500 rpm for several times until the PH value reached 6. After centrifugation, the precipitate was redispersed in DI water and sonicated for 1 h under the protection of Ar atmosphere at the temperature below 35 °C. After another centrifugation at 3500 rpm for 30 min, the dark green supernatant of the MXene nanoflakes was obtained. Among all etching methods, this technique can produce MXene nanoflakes with largest size, best quality (least defects), high electrical quality, and good environmental stability.[35] These features render the used MXene nanoflakes suitable for constructing optoelectronic devices. To construct the van der Waals heterostructure-based NIR photodetector, an n-type doped Ge substrate (resistivity: 0.1–6 Ω cm) covered with ∼300 nm plasma-enhanced chemical vapor deposition (PECVD)-grown SiO_2 insulting layer was used. Figure S1 in the supplementary material schematically shows the procedures for device fabrication. First, an open window (0.2×0.2 cm^2) defining the active region was obtained on the substrate by employing traditional UV photolithography, followed by etching the SiO_2 layer within the window with the help of a buffered oxide etching (BOE) solution. Then, a 5/50 nm double layer Cr/Au serving as the top electrode was deposited on the SiO_2 layer using a lab-made shadow mask via high-vacuum electron beam evaporation at room temperature. Afterward, the as-prepared $Ti_3C_2T_x$ MXene suspension (0.2 mg ml^{-1} in de-ionized water) was dropped on the substrate and naturally dried in air at room temperature. The above process was repeated several times to obtain an MXene nanoflake film with a thickness of about 800 nm [Fig. S2(a) in the supplementary material]. Finally, the In–Ga alloy acting as the bottom electrode was attached on the rear side of the Ge substrate. The electrical properties were measured on a Keithley 2636B source meter. Light emitting diodes (LEDs, Thorlabs products) with different wavelengths were employed as the light sources, and their light intensities were carefully calibrated by using a power meter (Thorlabs GmbH., PM 100D). The noise spectral density was recorded on a FS-Pro semiconductor parameter analyzer (Primarius Technologies). All measurements were performed under ambient conditions at room temperature.

A typical scanning electron microscopy (SEM) image of as-synthesized $Ti_3C_2T_x$ MXene before delamination is shown in Fig. 1(a). It was observed that the as-prepared product has accordion-like multilayered nanostructure with plenty of open edges, which suggests the fabrication of $Ti_3C_2T_x$ MXene. The SEM image of delaminated $Ti_3C_2T_x$ MXene nanoflakes dispersed atop a SiO_2/Si substrate is presented in Fig. 1(b). The result, together with a representative

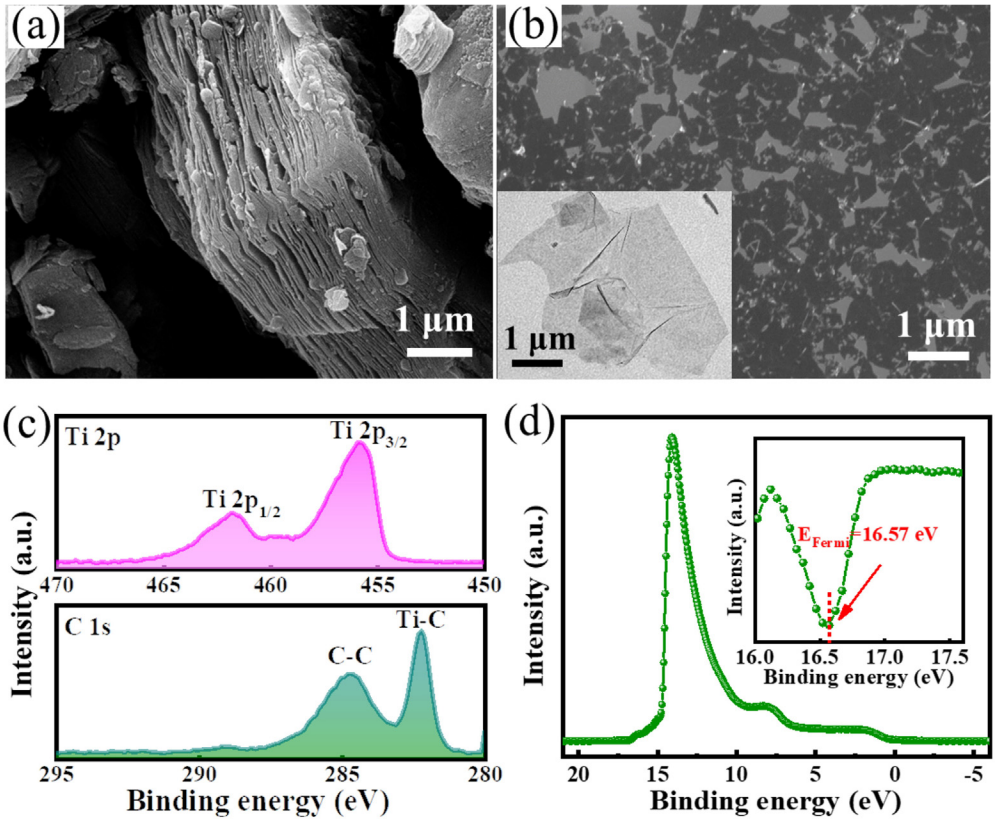

FIG. 1. (a) SEM image of $Ti_3C_2T_x$ MXene (multilayer nanoflakes) before delamination. (b) SEM and TEM (inset) images of delaminated $Ti_3C_2T_x$ MXene (few-layer nanoflakes). (c) Ti 2p (top panel) and C 1s (bottom panel) XPS spectra of $Ti_3C_2T_x$ MXene. (d) UPS spectrum of the $Ti_3C_2T_x$ MXene. Insets show the differential of Fermi edge (E_{Fermi}) region.

transmission electron microscopy (TEM) image [inset in Fig. 1(b)], shows that the few-layer nanoflakes typically have lateral sizes of hundreds of nanometers to several micrometers. Figure S2(b) displays a SEM image of the as-deposited MXene nanoflake film on a Ge substrate. Clearly, with the drop-casting technique, the MXene nanoflakes can form a compact, continuous, and relatively flat film without any pinholes, which is highly beneficial for the construction of high-quality heterostructures as well as high-performance photodetectors. Figure 1(c) reveals the x-ray photoelectron spectroscopy (XPS) results, where two apparent peaks at about 455.8 and 461.8 eV are assigned to the orbitals of Ti $2P_{3/2}$ and Ti $2P_{1/2}$, respectively (top panel), whereas two distinct peaks at about 282.2 and 284.7 eV are related to Ti–C bond and C–C bond, respectively (bottom panel).[21,36] In addition, the work function (W_F) of the $Ti_3C_2T_x$ MXene can be deduced by studying its ultraviolet photoelectron spectroscopy (UPS) spectrum, which is plotted in Fig. 1(d). The Fermi edge (E_{Fermi}) is determined to be ~16.57 eV by analyzing the differential of the curve of Fermi edge [inset in Fig. 1(d)], while the secondary electron cutoff edge (E_{cutoff}) is 0 eV due to the semi-metallic nature of MXene. Therefore, according to a commonly used equation, $W_F = 21.22 - (E_{Fermi} - E_{cutoff})$ (eV), the W_F of MXene is derived to be ~4.65 eV, which is close to the values of 4.60 and 4.62 eV in previous studies.[23,37]

Figure 2(a) displays a schematic diagram of the as-designed MXene/Ge 2D/3D van der Waals heterostructure-based NIR photodetector. We first studied the electrical characteristics of a representative heterostructure in darkness. As shown by the current–voltage (I–V) curve in both linear and semi-logarithmic scales [Fig. 2(b)], the heterostructure exhibits an apparent current rectifying behavior with a sizeable forward-to-reverse current ratio of about 10^2 at ±1 V. Such a value is comparable to or even higher than previously reported 2D TMD/Ge heterostructures.[11,14,38] The rectifying activity should originate solely from the heterojunction formed between MXene and Ge, in consideration of the good Ohmic contact between MXene and Au electrode as well as Ge and In-Ga alloy electrode (Fig. S3 in the supplementary material). Furthermore, the ideality factor n of the heterostructure was estimated to be ~1.46, by deducing the ln$I$–V curve [Fig. S4(a) in the supplementary material] according to an equation: $n = \frac{q}{K_B T}\frac{dV}{d\ln I}$, where q, K_B, and T refer to elementary charge, Boltzmann's constant, and Kelvin temperature, respectively.[39] The n value is close to that of an ideal diode ($n = 1$), and smaller than that of many 2D material/semiconductor heterostructures.[39,40] To gain more insights of the heterostructure, the barrier height (Φ_{BH}) was then calculated following the thermionic emission theory.[41] The diode properties can be characterized by the theory of majority carriers over a zero bias barrier from the Ge to MXene,

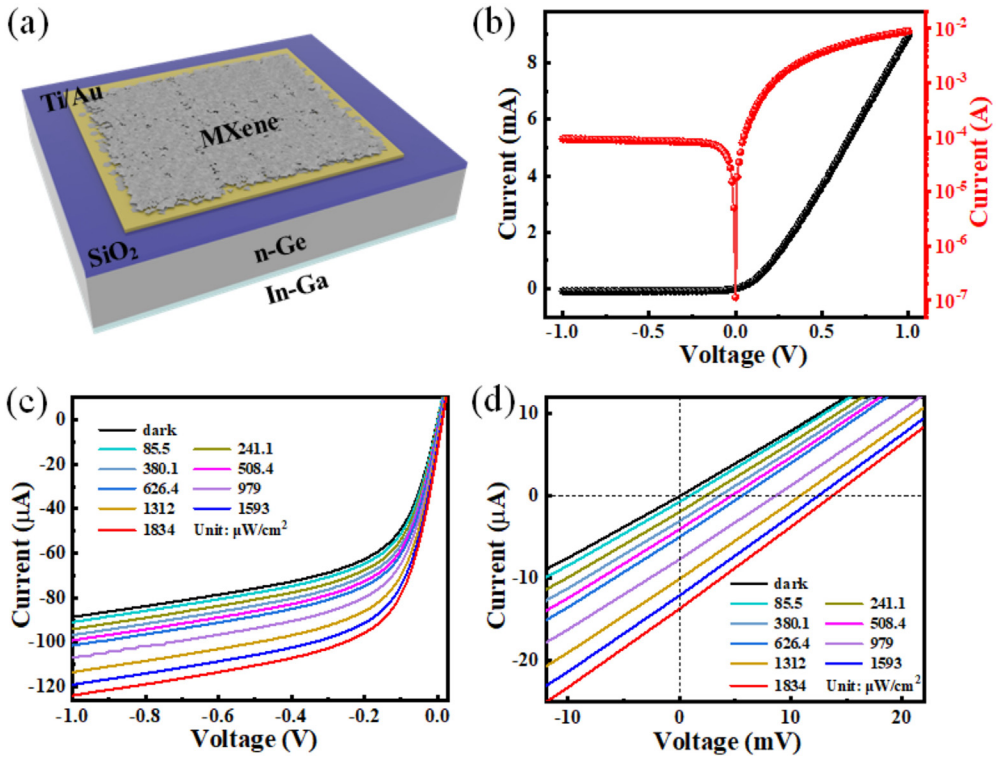

FIG. 2. (a) Schematic diagram of the MXene/Ge van der Waals heterostructure-based NIR photodetector. (b) Dark *I–V* curves of the MXene/Ge van der Waals heterostructure in linear and logarithmic coordinates. (c) *I–V* curves and (d) enlarged *I–V* curves of the device in darkness and under 1550 nm NIR light illumination with varied light intensities.

$$J(T,V) = J_S(T)\left[\exp\left(\frac{qV}{nk_BT}\right) - 1\right]. \quad (1)$$

The saturation current density J_S(T) is given by

$$J_S(T) = A^*T^2\exp\left(-\frac{q\Phi_{BH}}{k_BT}\right), \quad (2)$$

where A^* denotes the effective Richardson constant, which is 142.8 A cm^{-2} K^{-2} for n-Ge.[42] The J_S was deduced to be 7.01×10^{-4} A cm^{-2} from the ln *J–V* plot, as shown in Fig. S4(b) in the supplementary material. Accordingly, based on the above equations, the Φ_{BH} was calculated to be ~614.2 meV. The large current rectifying ratio, together with the small n and large Φ_{BH}, verified the high quality of the MXene/Ge van der Waals heterostructure.

The optoelectrical properties of the heterostructure-based device were characterized under 1550 nm NIR light illumination. Figure 2(c) plots the *I–V* curves in darkness and under light irradiation with varied intensities, implying a high sensitivity of the heterostructure to incident NIR light illumination. Careful analysis of the enlarged *I–V* curves shown in Fig. 2(d) indicates that the heterostructure actually exhibits an obvious photovoltaic behavior, i.e., a sizeable short-circuit current (photocurrent at zero bias) and an open-circuit voltage (photovoltage). Specifically, at a light intensity of 1.83 mW cm^{-2}, the photocurrent reaches 13.71 μA, and the photovoltage is 13.76 mV. Notably, such a photovoltaic effect empowers our device to serve as a self-driven NIR photodetector, which could greatly depress the energy consumption during operation. In addition, it is observed that photocurrents at both zero and reverse biases increase monotonically with the increase in light intensity, which can be attributed to more photoactivated charge carriers at elevated light intensity.

Next, we studied the transient photoresponse of the device under periodically switched NIR light illumination at zero bias. Figures 3(a) and 3(b) show transient photoresponses at different light intensities in the range of 2.4 μW cm^{-2}–2.98 mW cm^{-2}. Apparently, for all illuminating conditions, the device could show good and stable photoswitching behavior, i.e., it could be easily switched between low- and high-conductance states. The current on/off ratio attains up to ~430 at a light intensity of 2.98 mW cm^{-2}. Similarly, photocurrents rise gradually with increasing light intensity, which is in accordance with the *I–V* curves. Notably, even at a low light intensity of 2.4 μW cm^{-2}, the device can still show a distinguishable transient photoresponse, suggesting the possibility of the present NIR photodetector for weak light detection.

Furthermore, to better understand their relationship, the curve of photocurrent vs light intensity was fitted with a widely used power law: $I_{ph} \propto P_\lambda{}^\theta$, where I_{ph} and P_λ refer to the net photocurrent ($I_{ph} = I_{light}$-I_{dark}) and light intensity, respectively.[43,44] As shown in Fig. 3(c), careful fitting of the curve in a low light intensity region of 2.4–85.5 μW cm^{-2} and a high light intensity range of 85.5 μW cm^{-2}–1.83 mW cm^{-2} gives θ values of about 0.92 and 0.96, respectively. The θ value at the low light intensity range deviates a lot from the ideal value ($\theta = 1$), indicating the presence of nonnegligible

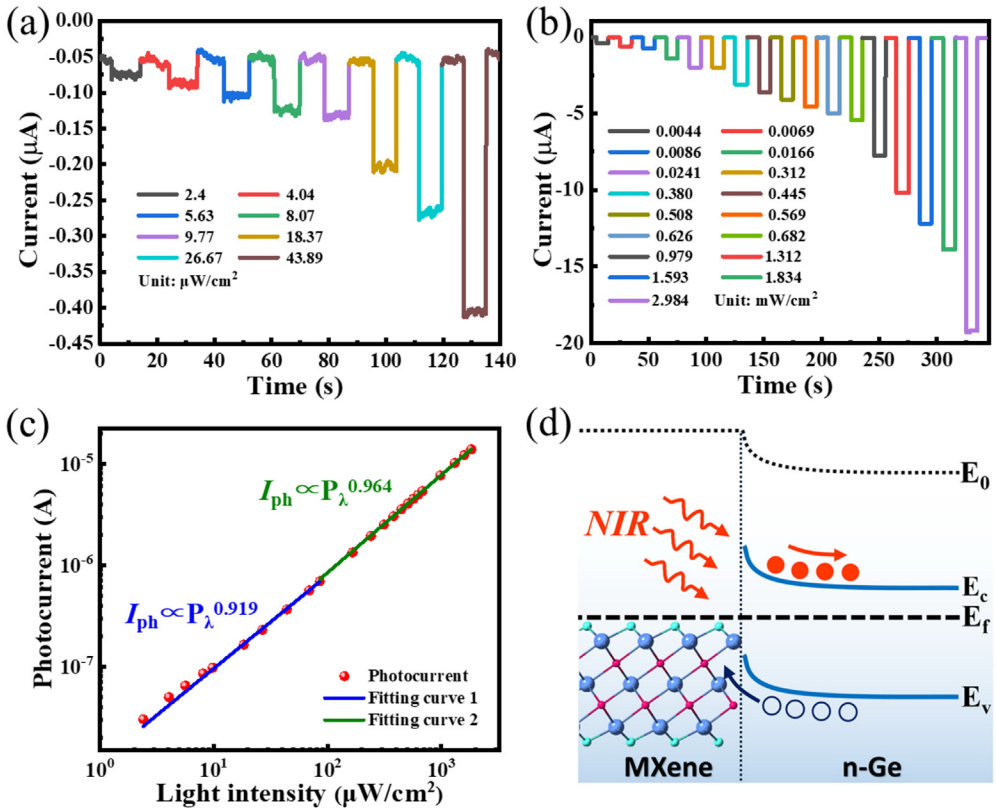

FIG. 3. (a) and (b) Transient photoresponse of the NIR photodetector under 1550 nm light illumination with different light intensities. (c) The curve of photocurrent vs incident light intensity. (d) Schematic diagram of the energy band diagram of the MXene/Ge van der Waals heterostructure upon NIR light illumination.

recombination loss caused by complex carrier recombination processes.[39] We also noted that the above evolution of the θ value with light intensity is different from that normally observed in other 2D material heterostructure-based photodetectors in which the θ is usually closer to the ideal value at a low light intensity range and becomes non-ideal at a high light intensity region.[45,46] The above phenomenon is likely caused by the existence of defects acting as the charge recombination centers in MXene films.[47] At low light intensity region, considerable photoinduced charge carriers were recombined before being collection, leading to non-linearity of the photocurrent with increasing light intensity. However, in a high light intensity range, the charge recombination centers are gradually saturated, and thus, the curve of photocurrent vs light intensity becomes linear.[48]

The optoelectronic behavior could be understood by analyzing the energy band diagram of the van der Waals heterostructure. When MXene is in contact with n-Ge, electrons will diffuse from Ge to MXene to acquire thermal equilibrium because of difference in their E_f (the E_f is ~−4.37 eV and ~−4.65 eV for n-Ge and MXene used here, respectively). This process induces the energy levels near the surface of Ge to bend upward and leads to the formation of a built-in electric field from n-Ge to MXene. As plotted in Fig. 3(d), when the heterostructure is shined by 1550 nm NIR light illumination, photoinduced electrons and holes generated within Ge are quickly separated by the built-in electric field. Subsequently, the electrons will transfer across the Ge and be collected by the In–Ga alloy, and the holes will be collected by the MXene and, finally, reach Au electrode, giving rise to the generation of photocurrent at zero bias.

To quantitatively compare the device performance, several vital performance parameters including photocurrent responsivity (R), external quantum efficiency (EQE), and specific detectivity (D^*) were then calculated. These parameters are usually given by the following formulas:[6]

$$R = \frac{I_{ph}}{SP_\lambda} = \left(\frac{q\lambda}{hc}\right) EQE, \tag{3}$$

$$D^* = \frac{(S\Delta f)^{1/2}}{NEP}, \tag{4}$$

$$NEP = \frac{\overline{i_n^2}^{1/2}}{R}, \tag{5}$$

where S, λ, h, c, NEP, Δf, and $\overline{i_n^2}^{1/2}$ refer to the effective device area (0.04 cm^2), incident light wavelength, Planck's constant, speed of light, noise equivalent power, bandwidth, and root mean square value of the noise current, respectively. Accordingly, the R was estimated to be ~314.3 mA W^{-1} at zero bias under a low light intensity of 2.4 $\mu W\,cm^{-2}$, corresponding to an EQE of 25.1%. The relatively high R value is comparable to that of many reported 2D material/semiconductor hybrid heterostructure-based photodetectors in literatures.[7,8]

In addition, the $\overline{i_n^2}^{1/2}$ at 1 Hz bandwidth was deduced to be $\sim 3.13 \times 10^{-13}$ A Hz$^{-1/2}$ by analyzing the noise spectral density at zero bias (Fig. S5 in the supplementary material), which gave a *NEP* of $\sim 9.96 \times 10^{-13}$ W Hz$^{-1/2}$. Therefore, the D^* was calculated to be $\sim 2.01 \times 10^{11}$ Jones according to Eq. (4).

We also explored the dependence of *R* value on the intensity of incident NIR light illumination. As plotted in Fig. 4(a), under both zero and reverse biases, *R* first declines gradually with increasing light intensity and then saturates as the light intensity exceeds $\sim 100\ \mu$W cm^{-2}. Such a dependence again verifies the existence of nonnegligible recombination loss at the low light intensity region as discussed above. In addition, we found that *R* could be greatly improved by simply increasing the reverse working bias. The dependence of *R* and *EQE* on working bias voltage is summarized in Fig. 4(b). It can be observed that both the values of *R* and *EQE* increase drastically as the working bias voltage increases from 0 V to −0.2 V and then increase slowly when the bias voltage is further increased to −1 V. In particular, at −1 V reverse bias, the *R* value is enhanced by more than 2 times and reaches a maximum of ~ 642.6 mA W^{-1}, which corresponds to an *EQE* value of 51.4%. The high *R* and D^* values render the present MXene/Ge heterostructure-based NIR photodetector very competitive, in comparison with similar devices in literatures and even commercial Ge-based NIR photodiodes (see Table I).

The spectral photoresponse, namely, the photoresponse vs the wavelength of incident light illumination, was further explored at zero bias. As shown in Fig. 4(c), the photoresponse first increases monotonically with increasing light wavelength from ∼250 to ∼1500 nm, reaching a peak photoresponse at around 1550 nm and then declines rapidly as the light wavelength is further increased. Such an evolution of photoresponse as a function of light wavelength can be correlated with the optical properties of the MXene/Ge van der Waals heterostructure. As shown in Fig. 4(d), the heterostructure displays strong photon absorption in the NIR wavelength region with the maximum absorption at around 1500–1600 nm. In addition, it should be noted that although the incorporation of MXene can greatly enhance the light absorption in the ultraviolet-visible wavelength range (about 250–700 nm), the photoresponse, however, is still relatively low in this wavelength region, similar to other 2D material/Ge photodetectors and commercial Ge-based photodiodes.[11,15] This result is probably due to severe charge recombination in the MXene film because of the presence of many defects, and thus, the photocarriers generated within MXene contribute negligibly to photocurrent. Therefore, in the present photodetector, the MXene serves as both an active layer to form a heterostructure and an electrode for charge collection, rather than a photoactive layer to generate photocarriers.

Response speed, as a pivotal parameter judging the ability of a photodetector to follow a fast varying photonic signal, was studied as well. A function generator was employed to power a 1550 nm NIR LED to produce light signal with different modulating frequencies, and the output photovoltage signal was recorded by a digital oscilloscope. Figures 5(a) and 5(b) show the transient photoresponse at the modulating frequencies of 5 and 19 kHz, respectively. Apparently,

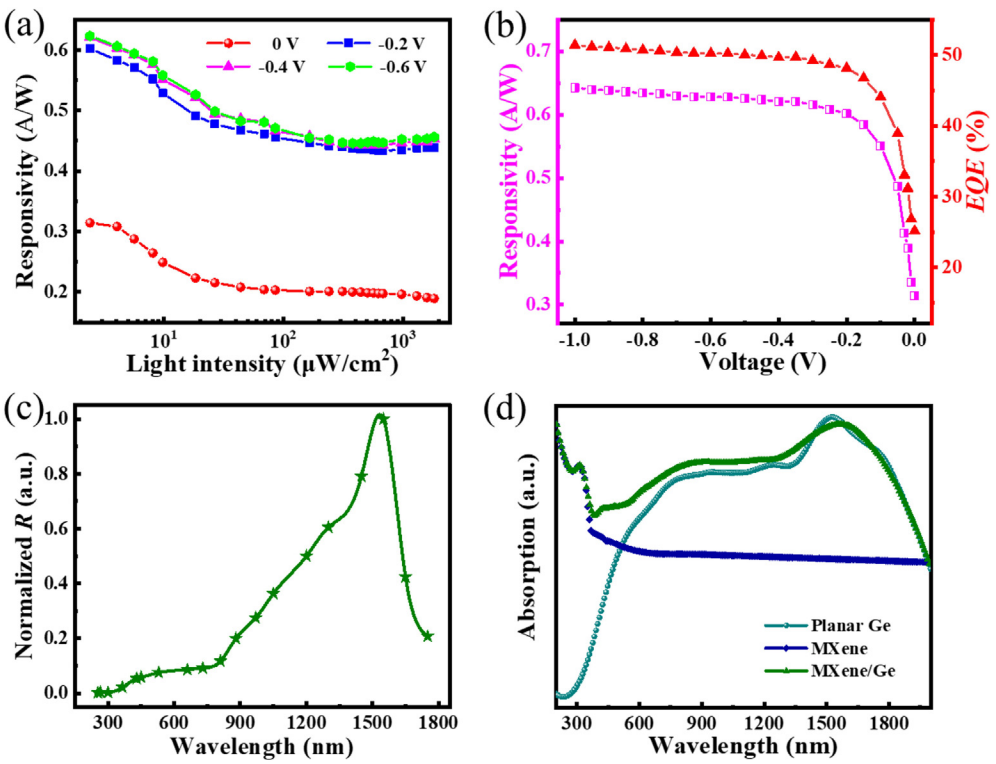

FIG. 4. (a) Responsivity as a function of light intensity at different working bias voltages. (b) Responsivity and EQE as functions of working bias voltage. (c) Spectral photoresponse of the photodetector in the wavelength of 250–1750 nm. (d) Absorption spectra of the MXene/Ge van der Waals heterostructure, MXene film, and planar Ge.

TABLE I. Comparison of photodetection performance and fabrication methods of the MXene/Ge heterostructure-based photodetector with other similar devices in previous studies.

Device structure	Fabrication methods	Responsivity (mA W^{-1})	Specific detectivity (Jones)	Response speed (μs)	Reference
Graphene/Ge	Transfer	51.8	1.38×10^{10}	23/108	10
$PtSe_2$/Ge	Transfer	602	6.3×10^{11}	7.4/16.7	11
$PdSe_2$/Ge	Transfer	530.2	1.45×10^{11}	26.4/38.5	14
Graphene/$PdSe_2$/Ge	Transfer	691	1.73×10^{13}	6.4/92.5	15
MXene/Si	Drop-casting	26.92	/	840/1670	31
MXene/Si	Spray-deposition	402	2.03×10^{13}	140/1600	32
MXene/GaN	Spray-deposition	284	7.06×10^{13}	7.55/1670	33
Commercial product (Ge-FDG03)	/	850	$\sim 10^{11}$	0.6/0.6	/
MXene/Ge	Drop-casting	648.6	2.01×10^{11}	17.6/13.6	This work

even at a high frequency of 19 kHz, the device still exhibits a prominent photo-switching characteristic with good repeatability, indicating a fast response speed. The relative balance $(V_{max}\text{-}V_{min})/V_{max}$ of the photoresponse vs the modulating frequency is summarized in Fig. 5(c). Notably, the relative balance can maintain 100% at initial stage and starts to decline only when the modulating frequency exceeds ~6 kHz. In addition, the 3-dB frequency, defined as the frequency at which point the photoresponse declines to 0.707 of the initial value, is deduced to be ~19 kHz. Furthermore, from an enlarged photoresponse curve, the rise and fall times (t_f and t_r) of response speed were estimated to be 17.6 and 13.6 μs, respectively [Fig. 5(d)]. The rapid response speed is faster than photodetectors made of MXene/Si and MXene/GaAs heterostructures,[29,31,32] and comparable to that of photodetectors based on MXene/GaN, MoS_2/Si, and $PdSe_2$/Ge heterostructures in literatures.[15,33,39]

The long-term stability and operation durability are vital for the practical applications of a photodetector. Figure 6(a) shows the

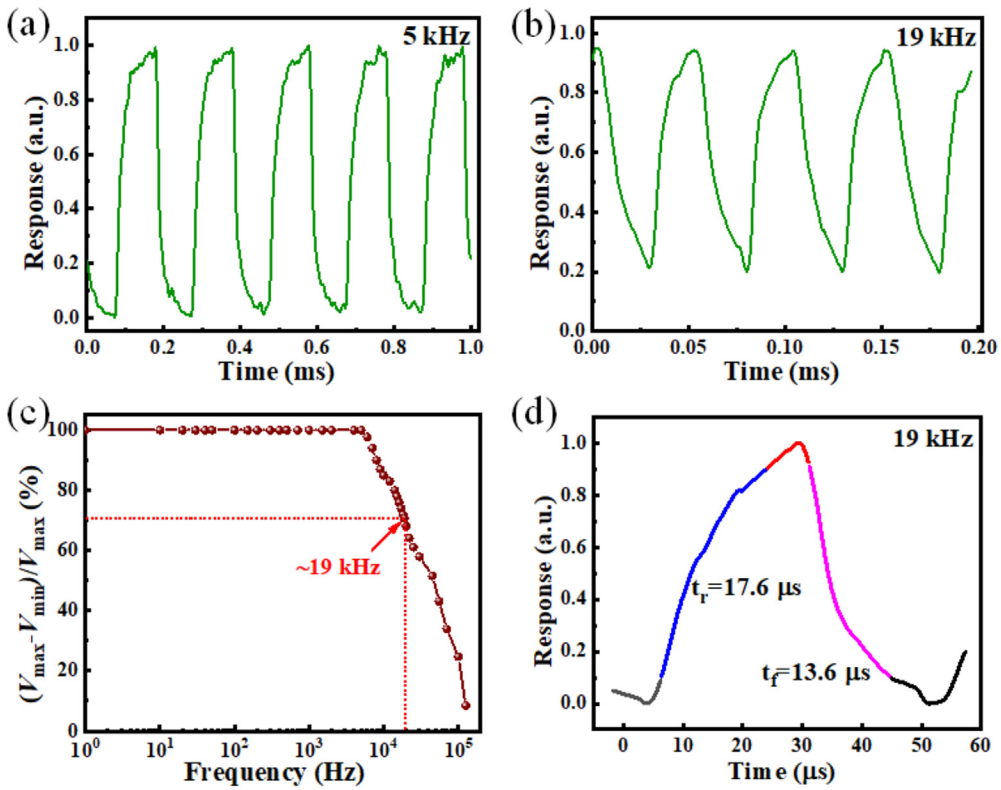

FIG. 5. Transient photoresponse of the NIR photodetector under 1550 nm light illumination at a frequency of (a) 5 and (b) 19 kHz. (c) Relative balance $(V_{max}\text{-}V_{min})/V_{max}$ vs incident light frequency, giving a 3 dB cutoff frequency of ~19 kHz. (d) An individual cycle of transient photoresponse at 19 kHz.

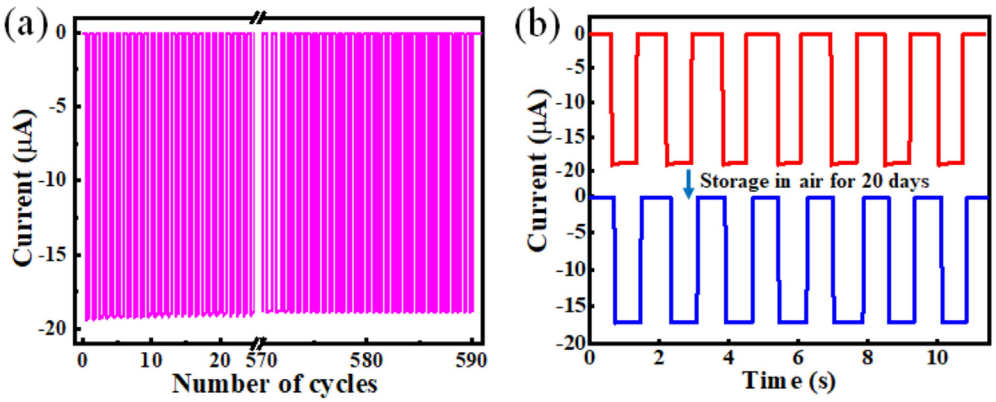

FIG. 6. Transient photoresponse of the MXene/Ge heterostructure-based NIR photodetector (a) during operation about 600 cycles and (b) before and after storage in ambient conditions for 20 days.

transient photoresponse of our device during operation over about 600 cycles, from which one can observe that the NIR photodetector retains its initial photoresponse properties with negligible degradation. Additionally, as shown in Fig. 6(b), after exposure in ambient conditions (relative humidity: about 30%–50% and temperature: 15–20 °C) for 20 days, the photo-switching behavior is well-preserved with excellent cycling capability. The photocurrent only degrades by about 8% of its initial value. The results imply respectable air stability and long-term durability of the present MXene/Ge van der Waals heterostructure-based NIR photodetector. The slight degradation might be caused by the surface oxidation of MXene nanoflakes via atomic defects in air, which could be avoided through some strategies such as device encapsulation.[32,49]

In summary, a self-driven NIR photodetector comprising a $Ti_3C_2T_x$ MXene/Ge 2D/3D van der Waals heterostructure has been constructed by employing a facile solution-based drop-casting technique. Upon 1550 nm NIR light illumination, the heterostructure-based device displays respectable device performance, including a decent photocurrent responsivity of ~314.3 mA W^{-1}, a high current on/off ratio of ~430, a large specific detectivity of ~2.01×10^{11} Jones, and a rapid response speed of 17.6/13.6 μs. Moreover, the photocurrent responsivity could be easily improved to as high as ~648.6 mA W^{-1} by applying a −1 V reverse working bias. The high photocurrent responsivity and specific detectivity are competitive with previously reported 2D material/Ge heterostructure-based NIR photodetectors and even commercial Ge-based NIR photodiodes. Moreover, the NIR photodetector demonstrates relatively good air stability and long-term operation durability. In consideration of the low-cost, mass-production ability of the MXene, simple device geometry, facile solution-based processability, and excellent device performance, this work, therefore, provides a convenient and unique approach for the fabrication of high-performance and cost-effective self-driven NIR photodetectors.

See the supplementary material for schematic diagram of the procedures for device fabrication, height profile of the deposited MXene nanoflake film, SEM image of the deposited MXene nanoflake film on the Ge substrate, *I*–*V* curves of Au-MXene-Au and In/Ga–Ge–In/Ga structures, ln*I*–*V* and ln*J*–*V* curves of the MXene/Ge heterostructure, and analysis of noise spectral density of the MXene/Ge heterostructure photodetector.

This work was financially supported by the National Natural Science Foundation of China (NSFC, Nos. 51902078 and 12004002), the Anhui Provincial Natural Science Foundation (No. 2008085MF205), the Fundamental Research Funds for the Central Universities (No. JZ2020HGTB0051), and the Hong Kong Polytechnic University (Project No. YW4Z).

AUTHOR DECLARATIONS

Conflict of Interest

The authors have no conflicts to disclose.

DATA AVAILABILITY

The data that support the findings of this study are available from the corresponding authors upon reasonable request.

REFERENCES

[1]G. Konstantatos, I. Howard, A. Fischer, S. Hoogland, J. Clifford, E. Klem, L. Levina, and E. H. Sargent, Nature **442**, 180 (2006).
[2]P. Martyniuk, J. Antoszewski, M. Martyniuk, L. Faraone, and A. Rogalski, Appl. Phys. Rev. **1**, 041102 (2014).
[3]J. Pei, J. Yang, T. Yildirim, H. Zhang, and Y. Lu, Adv. Mater. **31**, 1706945 (2019).
[4]J. Li, L. Niu, Z. Zheng, and F. Yan, Adv. Mater. **26**, 5239 (2014).
[5]J. Wang, H. Fang, X. Wang, X. Chen, W. Lu, and W. Hu, Small **13**, 1700894 (2017).
[6]C. Xie and F. Yan, Small **13**, 1701822 (2017).
[7]C. Liu, J. Guo, L. Yu, J. Li, M. Zhang, H. Li, Y. Shi, and D. Dai, Light. Sci. Appl. **10**, 123 (2021).
[8]M. Long, P. Wang, H. Fang, and W. Hu, Adv. Funct. Mater. **29**, 1803807 (2019).
[9]W. Chen, R. Liang, S. Zhang, Y. Liu, W. Cheng, C. Sun, and J. Xu, Nano Res. **13**, 127 (2020).
[10]L.-H. Zeng, M.-Z. Wang, H. Hu, B. Nie, Y.-Q. Yu, C.-Y. Wu, L. Wang, J.-G. Hu, C. Xie, F.-X. Liang, and L.-B. Luo, ACS Appl. Mater. Interfaces **5**, 9362 (2013).
[11]L. Wang, J.-J. Li, Q. Fan, Z.-F. Huang, Y.-C. Lu, C. Xie, C.-Y. Wu, and L.-B. Luo, J. Mater. Chem. C **7**, 5019 (2019).
[12]K. E. Chang, C. Kim, T. J. Yoo, M. G. Kwon, S. Heo, S. Kim, Y. Hyun, J. Il Yoo, H. C. Ko, and B. H. Lee, Adv. Electron. Mater. **5**, 1800957 (2019).

[13]R. Lu, C.-W. Ge, Y.-F. Zou, K. Zheng, D.-D. Wang, T.-F. Zhang, and L.-B. Luo, Laser Photonics Rev. **10**, 595 (2016).
[14]L. Luo, D. Wang, C. Xie, J. Hu, X. Zhao, and F. Liang, Adv. Funct. Mater. **29**, 1900849 (2019).
[15]D. Wu, J. Guo, J. Du, C. Xia, L. Zeng, Y. Tian, Z. Shi, Y. Tian, X. J. Li, Y. H. Tsang, and J. Jie, ACS Nano **13**, 9907 (2019).
[16]H. Xu, A. Ren, J. Wu, and Z. Wang, Adv. Funct. Mater. **30**, 2000907 (2020).
[17]X. Chen, Z. Shi, Y. Tian, P. Lin, D. Wu, X. Li, B. Dong, W. Xu, and X. Fang, Mater. Horiz. **8**, 2929 (2021).
[18]M. Hu, Z. Li, T. Hu, S. Zhu, C. Zhang, and X. Wang, ACS Nano **10**, 11344 (2016).
[19]D. Er, J. Li, M. Naguib, Y. Gogotsi, and V. B. Shenoy, ACS Appl. Mater. Interfaces **6**, 11173 (2014).
[20]B. Xu, M. Zhu, W. Zhang, X. Zhen, Z. Pei, Q. Xue, C. Zhi, and P. Shi, Adv. Mater. **28**, 3333 (2016).
[21]H. Fu, V. Ramalingam, H. Kim, C. Lin, X. Fang, H. N. Alshareef, and J. He, Adv. Energy Mater. **9**, 1900180 (2019).
[22]D. Pang, M. Alhabeb, X. Mu, Y. Dall'Agnese, Y. Gogotsi, and Y. Gao, Nano Lett. **19**, 7443 (2019).
[23]W. Deng, H. Huang, H. Jin, W. Li, X. Chu, D. Xiong, W. Yan, F. Chun, M. Xie, C. Luo, L. Jin, C. Liu, H. Zhang, W. Deng, and W. Yang, Adv. Opt. Mater. **7**, 1801521 (2019).
[24]L. Gao, C. Ma, S. Wei, A. V. Kuklin, H. Zhang, and H. Ågren, ACS Nano **15**, 954 (2021).
[25]K. Montazeri, M. Currie, L. Verger, P. Dianat, M. W. Barsoum, and B. Nabet, Adv. Mater. **31**, 1903271 (2019).
[26]J. Chen, Z. Li, F. Ni, W. Ouyang, and X. Fang, Mater. Horiz. **7**, 1828 (2020).
[27]S. Chertopalov and V. N. Mochalin, ACS Nano **12**, 6109 (2018).
[28]W. Ouyang, J. Chen, J. He, and X. Fang, Adv. Electron. Mater. **6**, 2000168 (2020).
[29]X. Zhang, J. Shao, C. Yan, X. Wang, Y. Wang, Z. Lu, R. Qin, X. Huang, J. Tian, and L. Zeng, Mater. Des. **207**, 109850 (2021).
[30]T. Jiang, Y. Huang, and X. Meng, Appl. Surf. Sci. **513**, 145813 (2020).
[31]Z. Kang, Y. Ma, X. Tan, M. Zhu, Z. Zheng, N. Liu, L. Li, Z. Zou, X. Jiang, T. Zhai, and Y. Gao, Adv. Electron. Mater. **3**, 1700165 (2017).
[32]W. Song, Q. Liu, J. Chen, Z. Chen, X. He, Q. Zeng, S. Li, L. He, Z. Chen, and X. Fang, Small **17**, 2100439 (2021).
[33]W. Song, J. Chen, Z. Li, and X. Fang, Adv. Mater. **33**, 2101059 (2021).
[34]L. Luo, Y. Huang, K. Cheng, A. Alhassan, M. Alqahtani, L. Tang, Z. Wang, and J. Wu, Light. Sci. Appl. **10**, 177 (2021).
[35]Q. Wang, S. Wang, X. Guo, L. Ruan, N. Wei, Y. Ma, J. Li, M. Wang, W. Li, and W. Zeng, Adv. Electron. Mater. **5**, 1900537 (2019).
[36]S. A. Shah, T. Habib, H. Gao, P. Gao, W. Sun, M. J. Green, and M. Radovic, Chem. Commun. **53**, 400 (2017).
[37]Z. Wang, H. Kim, and H. N. Alshareef, Adv. Mater. **30**, 1706656 (2018).
[38]D. Wu, J. Guo, C. Wang, X. Ren, Y. Chen, P. Lin, L. Zeng, Z. Shi, X. J. Li, C.-X. Shan, and J. Jie, ACS Nano **15**, 10119 (2021).
[39]L. Wang, J. Jie, Z. Shao, Q. Zhang, X. Zhang, Y. Wang, Z. Sun, and S.-T. Lee, Adv. Funct. Mater. **25**, 2910 (2015).
[40]C. Xie, Y. Wang, Z. X. Zhang, D. Wang, and L. B. Luo, Nano Today **19**, 41 (2018).
[41]X. An, F. Liu, Y. J. Jung, and S. Kar, Nano Lett. **13**, 909 (2013).
[42]T. Nishimura, X. Luo, S. Matsumoto, T. Yajima, and A. Toriumi, AIP Adv. **9**, 095013 (2019).
[43]X. Li, M. Zhu, M. Du, Z. Lv, L. Zhang, Y. Li, Y. Yang, T. Yang, X. Li, K. Wang, H. Zhu, and Y. Fang, Small **12**, 595 (2016).
[44]Y. Zhang, P. Huang, J. Guo, R. Shi, W. Huang, Z. Shi, L. Wu, F. Zhang, L. Gao, C. Li, X. Zhang, J. Xu, and H. Zhang, Adv. Mater. **32**, 2001082 (2020).
[45]C. Xie, L. Zeng, Z. Zhang, Y. H. Tsang, L. Luo, and J. H. Lee, Nanoscale **10**, 15285 (2018).
[46]M. Ma, H. Chen, K. Zhou, C. Xie, Y. Liang, L. Wang, C. Wu, W. Yang, J. Guo, and L. Luo, J. Mater. Chem. C **9**, 2823 (2021).
[47]K. A. Papadopoulou, A. Chroneos, D. Parfitt, and S.-R. G. Christopoulos, J. Appl. Phys. **128**, 170902 (2020).
[48]D. Kufer, I. Nikitskiy, T. Lasanta, G. Navickaite, F. H. L. Koppens, and G. Konstantatos, Adv. Mater. **27**, 176 (2015).
[49]W. Cui, Z.-Y. Hu, R. R. Unocic, G. Van Tendeloo, and X. Sang, Chin. Chem. Lett. **32**, 339 (2021).